Efficient Implementation of MINT-Based Chemiresistor Arrays for Artificial Olfaction

Michele Galvani, Alejandro López-Moreno, Natalia Martín Sabanés, Sylwia Parzyszek, Michele Zanotti, Sonia Freddi, Emilio M. Pérez, and Luigi Sangaletti

Efficient Implementation of MINT-Based Chemiresistor Arrays for Artificial Olfaction.

Michele Galvani[†], Alejandro López-Moreno[‡], Natalia Martín Sabanés[‡], Sylwia Parzyszek[‡], Michele Zanotti[†], Sonia Freddi[†⊥], Emilio M. Pérez,*[‡] Luigi Sangaletti*[†]

[†] Surface Science and Spectroscopy Labs @ I-LAMP, Department of Mathematics and Physics, Università Cattolica del Sacro Cuore, via della Garzetta 48, 25113 Brescia (Italy)

[‡] IMDEA Nanociencia, Faraday 9, 28049 Madrid (Spain)

[⊥] Present address: Institute for Photonics and Nanotechnologies (IFN) - Consiglio Nazionale delle Ricerche (CNR) L-NESS laboratory, via Anzani 42, 22100 Como (Italy)

Email: luigi.sangaletti@unicatt.it; emilio.perez@imdea.org

KEYWORDS: carbon nanotubes, MINTs, electronic nose, gas sensing, Raman, artificial olfaction, PCA, UMAP, machine learning

ABSTRACT: We demonstrate the possibility to use an array of MINTs based chemiresistors for a selective detection of VOCs at room temperature. Four new types of MINTs with different functional groups ($MINT_{ALKENE}$ (X:-$CH{=}CH_2$), $MINT_{COOMe}$ (X:-COOMe), $MINT_{COOH}$ (X:-COOH), $MINT_{CH2OH}$ (X:-CH_2OH)) were specifically synthesized to prepare a set of six sensing layers which included, in addition to the new MINTs, a pristine SWNT layer and a $MINT_{XYLENE}$ layer. The functionalized sensing layers have been tested by exposing them to NH_3, NO_2, EtOH, IPA, acetone, benzene, and NaClO vapours in the ppm range. We show that MINT functionalization enhances response to analytes with respect to pristine SWNTs. When assembled into an array, our sensing layers can operate at room temperature as an electronic nose, disclosing the possibility to use these layers in low power consumption, wearable devices. Correlation plots, PCA, and UMAP analysis show that a remarkable discrimination of ammonia with respect to interfering gases can be reached by the e-nose. Gas mixtures were also discriminated, as shown for NH_3/ethanol, acetone/ethanol, and isopropanol/acetone mixtures that are relevant in view of breathomics applications. The efficient preparation method of sensing layers allows for an improvement of performance, as shown for one of the best performing chemiresistors in the set, resulting in a sensitivity increase (up to 10x) and dramatic reduction of response and recovery times.

1.Introduction

Single-walled carbon nanotubes (SWNTs) are particularly well-suited for gas sensing **[1, 2]** due to their unique properties, which include (i) a high surface-to-volume ratio, thus providing more active sites for target gas molecules to interact with the sensor material; (ii) rapid response to gas exposure and swift recovery to pre-exposure conditions **[3]**; (iii) possibility of miniaturization and integration into microelectronic devices, enabling the development of compact and portable sensors; (iv) environmental stability, which ensures the durability and longevity of the sensors even in harsh environmental conditions; (v) low power consumption due to the possibility to operate at room temperature, which makes them ideal for portable and battery-operated e-nose devices. In particular, SWNT-based e-noses **[4, 5]** represent a cutting-edge technology that leverages the unique properties of SWNTs to create sensitive and selective sensor systems capable of mimicking human olfactory functions in various applications **[6]**.

For any sensing application, functionalization of SWNTs is known to be a key strategy to enhance performance, particularly in terms of selectivity. Derivatization strategies so far have been based on either covalent **[7]** or supramolecular chemistry **[8]**, and chemiresistive layers based on functionalized SWNTs have been tested **[9, 10]**.

An interesting alternative for the derivatization of SWNTs is the formation of rotaxane-like mechanically interlocked derivatives of SWNTs (MINTs).**[11]** In MINTs, macrocyclic molecules are threaded through SWNTs, providing a means to attach chemical functionalities to SWNTs in a stable manner without affecting the intrinsic structure of the SWNTs. This combination of stability, dynamic nature and structural integrity provided by the mechanical bond **[12]** has made MINTs relevant for a variety of applications. For example, MINTs have been shown to serve as superior fillers in composite materials **[13-15]** as qubits **[16]** and in (electro)catalysis, **[17-19]** outperforming both pristine SWNTs and supramolecular compounds of identical chemical composition.

Importantly, several synthetic strategies towards MINTs have been described, including our ring-closing metathesis clipping method **[20]**, the direct threading of preformed macrocycles **[21]**, the use of metal-coordination **[22, 23]** and dynamic covalent chemistry **[24, 25]**. Recently, a strategy based on mechanochemistry has enabled the synthesis of MINTs in multigram scale, facilitating their real-world applications.**[26]**

Among possible applications, those dealing with gas-surface interactions in MINTs have scarcely been explored. In particular, pioneering work by the Komatsu group has provided proof-of-concept for the use of MINTs in chemiresistive gas sensing.**[27]** The use of MINTs in sensing arrays (i.e. e-noses) is completely unexplored to date.

Here, we systematically explore the possibility to use MINTS for chemiresistive gas sensing, both as single layers and as sensor arrays to be operated as electronic noses for artificial olfaction.

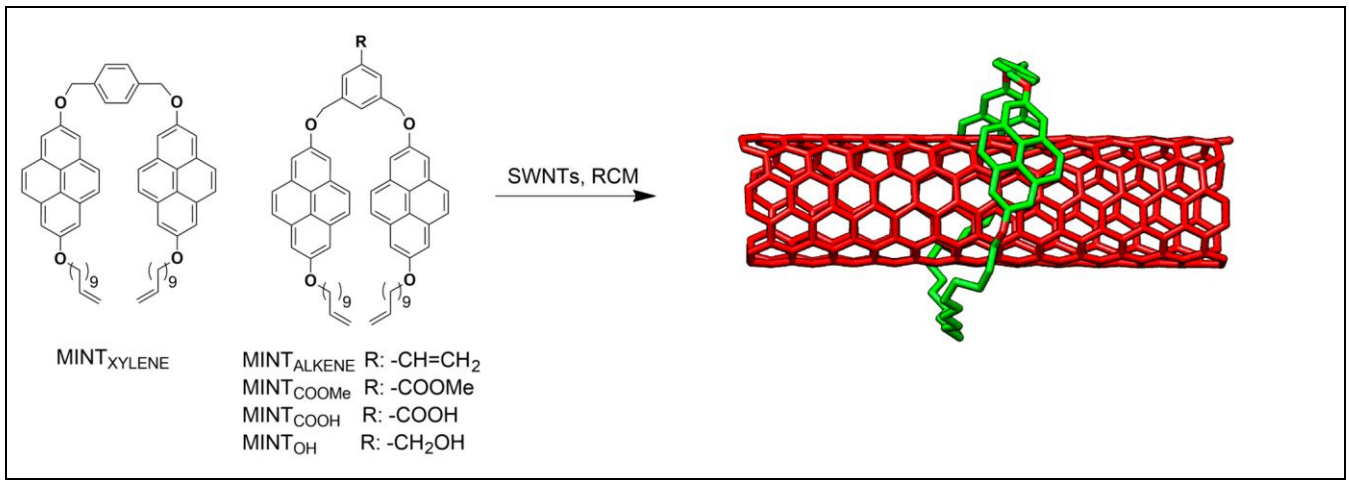

Figure 1. Chemical structures of U-shapes used in the preparation of MINTs and the energy-minimized (MM+) model of MINT$_{XYLENE}$

To achieve this, we synthesized four new types of MINTs with different functional groups (X), namely: MINT$_{ALKENE}$ (X:-CH=CH$_2$), MINT$_{COOMe}$ (X:-COOMe), MINT$_{COOH}$ (X:-COOH), MINT$_{OH}$ (X:-CH$_2$OH) (Figure 1). We show that the use of MINTs clearly improves the sensitivity of chemiresistors compared to pristine SWNTs, and we can evidence the best performing layers. Furthermore, the array of sensors displays a remarkable discrimination capability to detect ammonia (NH_3) vs. a set of possible interfering gas molecules, such as ethanol (EtOH), isopropanol (IPA), acetone, and sodium hypochlorite (NaClO).

Among possible target gas molecules, NH_3 is usually regarded as a test analyte for benchmarking of SWNT layers performance. Furthermore, the need to monitor ammonia is widespread **[28]**, spanning many application fields, such as (i) environmental monitoring, where NH_3 in the air is detected for environmental protection and pollution control **[29]**; (ii) industrial safety, where ammonia levels in industrial settings are detected to prevent hazardous conditions; (iii) agriculture, to manage ammonia emissions in agricultural practices; (iv) healthcare, as breath analysis for diagnosing certain medical conditions associated with elevated ammonia levels **[30- 34]**. Indeed, in view of future application of our e-Nose we finally test our system on detection of NH_3/ethanol, but also on acetone/ethanol, and isopropanol/acetone mixtures, that are of interest in the field of breathomics **[35-37]**.

2. Material and methods:

2.1 Synthesis of MINTs

MINTs were synthesized by mechanochemical methods [26] using a commercially available ball mill (Fritsch PULVERISETTE 7) equipped with stainless steel reactors and balls. 50 mg of SWNTs, 0.48 µmol/mg U-shape (see SI for synthesis information) and 0.1 µmol/ U-Shape µmol of Grubbs catalyst 2nd gen. were place in a 20 mL stainless steel reactor containing 2 stainless steel balls (10 mm on diameter) and 0.4 mL of toluene. The mixture was milled 5 min at 150 rpm. After each milling experiment, the resulting powder was collected and the unreacted U-shapes, and Grubbs' catalyst were removed by three washes in DCM, in which we suspend the product in 20 mL of DCM with 5 minutes bath sonication and then filter the solid through a 0.2 µm pore PTFE membrane. All samples used in this study were adequately characterized by standard methods, including thermogravimetric analysis (TGA), Raman, UV–vis–NIR (see Figures S1-S6 and Table S1 in SI). Mass density of U-shapes in MINTs powders are listed in Table 1.

2.2 Chemiresistor preparation

MINTs suspensions (suspended in a 1% SDS-D_2O solution with a concentration of 1 mg/ml) were dropcasted on 13.4x7.0 mm^2 ceramic alumina substrates with Ag interdigitated electrodes (IDE: line width 200 µm, line spacing 200 µm). After the deposition, the resistance of each chemiresistor was measured. The values are shown in **Table 1**. Once the potential difference was applied, a reduction of these values due to sensors conditioning was observed. In the cases of the lowest resistive sensors (SWNTs and MINT$_{OH}$) a 1000 Ω load resistance was added in series to limit the amount of current flowing in the sensors to avoid sensing layer degradation, and a constant voltage drop was applied to all the sensing layers of the array.

Table 1: Sample identification

Label	R (Ohm)	Thickness (µm)	MINT mass %	A (x10^{-4})	n
SWNTs	652±1	12.0±0.5	-	4 ± 1	0.32 ± 0.09
MINT$_{XYLENE}$	2829±1	8.0±0.5	24	16 ± 4	0.50 ± 0.10
MINT$_{ALKENE}$	1416±1	10.0±0.5	25	27 ± 3	0.32 ± 0.06
MINT$_{COOMe}$	2317±1	5.0±0.5	25	24 ± 3	0.46 ± 0.05
MINT$_{COOH}$	1677±1	3.0±0.5	23	16 ± 2	0.41 ± 0.06

$MINT_{OH}$	1159±1	4.0±0.5	26	8 ± 2	0.30 ± 0.10

Table 1: Sample identification, mass density of U-shapes in MINTs powders, sensing layer resistance (R, Ohm) after the drop-casting process on interdigitated electrodes, minimum thickness (μm), as measured by profilometry, A and n parameters resulting from the fitting of the NH_3 calibration curves with a Freundlich isotherm.

2.3 E-nose assembly and set up for gas sensing measurements

Gas exposure effects on the resistivity of the SWNT layers were recorded at room temperature inside a chamber with a volume of 30 cm^3. Each exposure lasted about 30 seconds, with a recovery time of about one minute. At the end of the exposure the chamber was properly evacuated, before proceeding to further exposures.

During all exposures, a constant voltage of 0.1V was applied across the sensing layer. Current intensity data were recorded with a PalmSens4 console, with a multiplexing unit, at a sampling frequency of 4Hz.

Once the current intensity was measured, the response S (Eq. 1) was calculated as the relative current change (I_{gas}-I_0) with respect to the current flowing across the layer before exposure to target gas (I_0), namely:

$$S = \frac{|I_{gas} - I_0|}{I_0} = \frac{\Delta I}{I_0} \qquad [1]$$

Gas sensing properties were explored by exposing the sensing layers to the following set of analytes diluted in air: NH_3 (1-100 ppm), NO_2 (2-8 ppm), acetone, ethanol, and IPA (100-600 ppm), NaClO (100-400 ppm), benzene (5 ppm).

2.4 Data analysis.

Data analysis was carried out through Python, using the scikit-learn library. Based on the dataset obtained by exposing the six sensing layers to target gas molecules, correlation matrices, Principal Component Analysis (PCA) **[38]** and Uniform Manifold Approximation and Projection (UMAP) **[39]** data representation and reduction were considered.

3. Experimental results

3.1 Sensing layer characterization

SEM analysis resulted (**Figure 2 - top panel**) in a relatively thick SWNT layer uniformly distributed on the IDE substrate. The layer thickness, estimated by line-scan AFM mapping (not shown here), ranges from 3 to 12 μm. Data for each sample are reported in **Table 1**. Images of samples collected with an optical microscope and results of profilometric measurements are shown in Fig. S7 of the SI. Thickness data reported in Table 1 refer to the central area of each sample, as we observe a noticeable coffee-ring effect as expected for drop-casted samples.

Representative Raman spectra of the six layers in the 1250-2800 cm^{-1} wavenumber range are shown in the **bottom-left panel of Figure 2**. MicroRaman maps have been collected from each of the six layers by sampling about 100 points on the sample surface. Maps were collected both from SWNTs in contact with the bare alumina substrate and with the Ag electrodes. We did not detect significant differences among the two different maps. The statistics of the G' peak wavenumber for all samples, both in air and in the presence of NH_3, is shown in the **bottom-right panel of Figure 2**. An overall decrease of nearly 3 cm^{-1} for the MINT layers was registered with respect to the pristine SWNTs.

3.2 Gas sensing

Dynamic response

The dynamic response to selected target gas molecules is shown in **Figure 3-a**. For each of the 6 sensing layers the ΔI/I signal is plotted vs time for a set of exposures (30 seconds separated by 60 seconds of recovery). The bottom panel displays details of a single exposure to each gas for all samples.

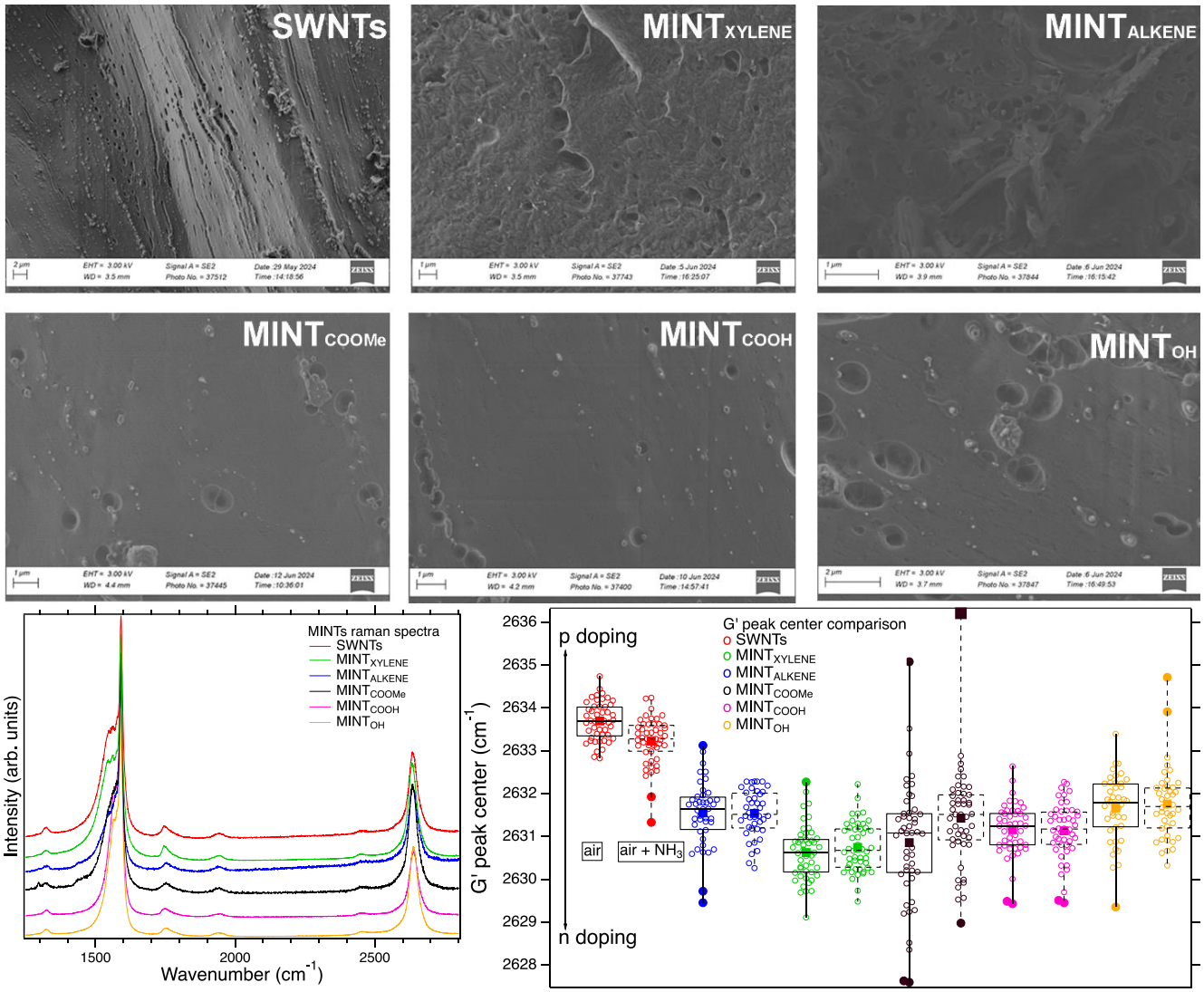

Figure 2: Top panel: SEM imaging of the six sensing layers. Bottom left panel: Representative Raman spectra for the six sensing layers. Bottom right panel: Statistical analysis of G' peak position extracted from the microRaman maps collected in air and under NH_3 exposure. For each sensing layer, distribution of G' peak wavenumbers in air and in air+NH_3 are shown in the left and right box plots, respectively.

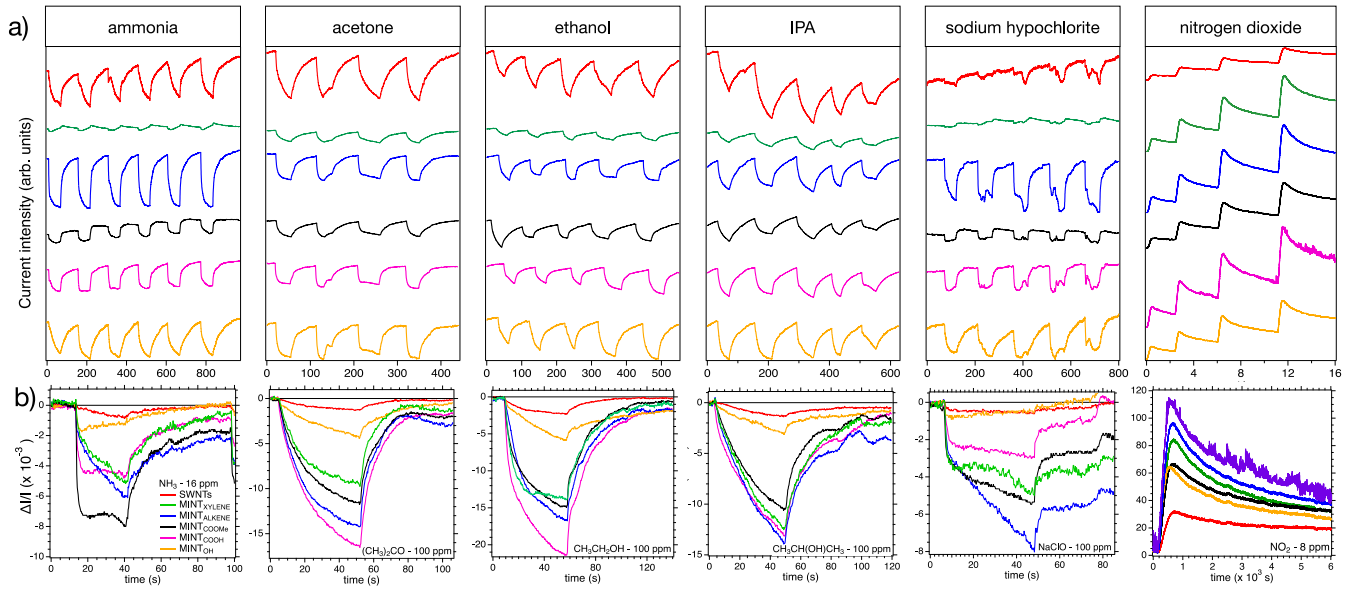

Figure 3. Top panel: Sequence of dynamic responses to target gas molecules: a) NH_3 (16 ppm); b) acetone (>100 ppm); c) EtOH (>100 ppm); d) IPA (>100 ppm); e) NaClO (>100 ppm), NO_2 (2-8 ppm). For all data a vertical offset has been applied to provide a clear representation of each dynamic response curve. Bottom panel: detailed view of single exposures, comparing the dynamic response of the 6 sensing layers to the 5 analytes.

The electronic noise is about 1μA, which is negligible with respect to the signal variation due to gas adsorption, while larger fluctuations that can be observed are due to chamber fluid dynamics during the gas exposure. As can be noticed, the sensing layers show a different lineshape, response time and recovery time in the dynamic response.

Apart from the NO_2 case, the dynamic behavior displays a current decrease in all exposures, i.e. resistivity increases upon adsorption of all target gas molecules. This suggests an overall p-doping of the SWNT sensing layer if we assume that all analytes are electron donors. p-doping of SWNTs is expected mainly due to the presence of oxygen (and water vapor) in the atmosphere **[40, 41]**. Actually, p-doping is confirmed by the results obtained for NO_2 exposure, where all samples display and increase of current upon gas adsorption, as the oxidizing behavior of NO_2 is expected to increase the number of holes in the SWNTs.

Finally, no evidence of sensors response was registered for benzene exposures, which is also regarded as a VOC in breathomics **[42]**. This result is to some extent expected, as reaction of benzene with bare SWNTs involves weak Π-stacking interactions and electronic properties of SWNTs were found to be virtually unchanged upon benzene adsorption [**43**]. Data on benzene are displayed in Fig. S8 of the SI.

Further information from this issue can be drawn from Raman data, where the G' mode of the pristine layer was found at 2633 ± 0.3 cm^{-1}, while for all the other samples a downshift of about 3 cm^{-1} was registered over a statistical sample of about 100 spectra for each layer (Figure 2). As discussed in reference **[44]**, the wavenumber of the G' Raman mode depends on the SWNT doping. Hence, interaction with an electron acceptor (p doping) causes a shift of the center of the peak towards higher wavenumbers. On the contrary, an electron donor (n doping) causes a shift to lower wavenumbers **[44]**. For pristine SWNTs with diameter d ≈ 1.5 nm, the G' peak is expected at $x_{G'}$ (cm^{-1}) = 2420 + 106E_{laser} (eV) **[45]**. In the present case, we have $x_{G'} \simeq 2627$ cm^{-1} for SWNTs with a diameter (1.6 ± 0.4 nm **[46]**) very close to the reference value of 1.5 nm. On this basis, SWNTs with G' peak centered at higher wavenumbers can be regarded as p-doped, as is the present case, consistently with the decrease of the chemiresistors current upon exposure to reducing NH_3. Likewise, MINTs are still found on the p-doped side (G' modes are all above 2627 cm^{-1}) but, as compared to the pristine layer, they can be regarded as less p-doped.

Chemiresistors in the array showed a different response to the same concentration of each of the target gas molecules. The response is measured by considering the largest change of conductivity during each exposure. These responses for each of the 6 analytes are shown in **Figure 4**, where the maximum of |ΔI/I| is displayed for the six sensing layers and for all analytes. It can be noticed that "$MINT_{XYLENE}$", "$MINT_{ALKENE}$", "$MINT_{COOMe}$" and "$MINT_{COOH}$" seem to show a higher response for all target gases, while the bare SWNT layer always displays the lowest response. This demonstrates that functionalization significantly improves the sensitivity of functionalized SWNT layers. Furthermore, when properly normalized to the analyte concentration, the sensing layers are found to be selective towards NH_3 as a reducing molecule, and NO_2 as an oxidizing molecule.

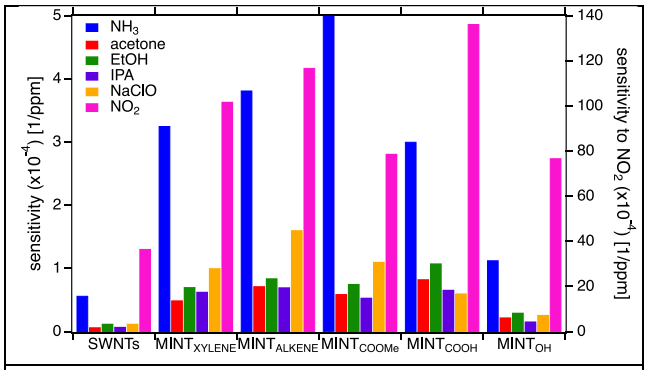

Figure 4: Chemiresistors response normalized to the concentration of analytes. Left to right: NH_3 (cyan); acetone (red); EtOH (green); IPA (blue); NaClO (orange); NO_2 (magenta). NO_2 sensitivity scale is on the right axis. |ΔI/I| absolute values were considered for all samples

It is important to underline how the array shows a different responses pattern to the different target gases. In fact, some sensors seem to be more sensitive to specific chemical species than other. For instance, "$MINT_{COOH}$" shows the largest response to acetone and ethanol, while "$MINT_{COOMe}$" is the best performing in the case of NH_3 exposure, "$MINT_{ALKENE}$" is the best for IPA, and "$MINT_{COOH}$" for NO_2. This "specialization" plays a fundamental role in their use as an electronic nose.

Calibration curves for NH_3

Exposing the array to a set of different NH_3 concentrations in the 1-16 ppm range allowed us to build the calibration curves for NH_3 (**Figure 5, left panel**). This graph relates each sensor response to the analyte concentration. Its shape is intrinsically related to the surface adsorption mechanism (see e.g. **[47]**). In this case, we fit the experimental data with a Freundlich isotherm **[48]**:

$$S(c) = y_0 + Ac^n \qquad [2]$$

where *S* is the sensing layer response and *c* the analyte concentration (**Figure 5-right panel**). Since at concentration equal zero no response is measured, the y_0 parameter is set at 0. The NH_3 concentration values have been measured using a properly calibrated Figaro TGS2602 sensor. From **Figure 5, left panel**, it is possible to evaluate the response of all layers to NH_3, with the lowest response given by the SWNTs sensing layer and the highest response given by $MINT_{COOH}$. The fitting results (**Table 1**) confirm this trend.

On the basis of these data, the limit-of-detection (LOD) for ammonia has been calculated. We estimated the LOD by calculating the signal standard deviation σ (in the constant-current region before exposure) and then by retrieving the corresponding concentration using the estimated calibration curve equation. In order to take into account possible higher current fluctuations, a value of 3σ is considered. Therefore, LOD has been calculated as $[LOD] = (3\sigma/A)^{1/n}$. Error bars on the A and n fit parameters yield relatively large error bars on LODs, but the overall LOD for each sample is found to be of the order of tens of ppb, well below the minimum concentration (1 ppm) experimentally explored. LODs and δ_{LOD}/LOD (%) for each active layer during ammonia sensing are reported in Table S2 of the SI file.

Humidity effects and stability over time

Furthermore, for the case of ammonia detection, data have been collected under different R.H. conditions (Fig. S9 of the SI) as the effect of humidity is relevant for specific applications such as breathomics, where ammonia can be regarded as a biomarker **[32]**. R.H. is known to affect the overall response of the sensing layer **[49]**. Usually, sensitivity to ammonia increases with RH, as predicted by computational studies of [**50**]. Measurements on the present sensing layers have been carried out at R.H.= 20, 30, 40, 50, and 60 %. Respect to **[49]**, we observe an increase of the response up to about R.H. = 30-40 %, but beyond this limit we observe a decrease of response that we ascribe to a competition for adsorption sites between NH_3 and H_2O, that might be favored by the morphology of the present layers, much thicker that those reported in ref. **49**.

Finally, stability over time and repeatability have been considered by collecting new sequences of exposure 9 months later with respect to those shown in Figure 3. Data are shown in Fig. S10 of the SI file. Sensor resistance values over time are reported in Table S3 of the SI file. After 9 months, the baseline resistance values decreased by 18.5 % to 36.8 % of the starting values.

Sensing mechanisms

The experimental evidence presented so far allow us to discuss the possible mechanism underlying gas-MINT layer interactions. At the level of analyte-MINT interaction, the overall response of the sensing layers can be related to charge transfer between this molecule and the MINTs. With the MINTs being initially p-doped, we register an increase of majority charge carriers (holes) determined by the absorption of the oxidizing NO_2 which turns into an increase of the measured current. A detailed presentation of the results of exposures to NO_2 is reported in Fig. S11 and Table S4 of the SI. Consistently with findings for NO_2, exposure to reducing NH_3 determines a decrease of holes due to electron donation, and therefore a decrease of the current intensity.

Beyond this fundamental mechanism, it is important to consider other effects in the overall response of sensing layers that can be related to the morphology of the layer itself.

After synthesizing MINTs, the amount of functionalization with respect to the total mass was measured using TGA (see Fig. S1 of the SI). The results (reported in detail in **Table 1** show that approximately 25% of the total MINTs mass is represented by the functionalization. This means that for each nanotube, a high number of interlocked macrocycles is present –approximately one macrocycle per 300 SWNT C atoms. This fact has at least two main consequences:

i) at first, we suppose that a high coverage of the SWNTs with macrocycles reduces the tendency of SWNTs to form aggregates. This would favor a higher MINTs spreading on the substrate and therefore a higher active surface for gas interaction. This is consistent with the increase of the response of MINTs with respect to bare SWNTs. Furthermore, the increase of dispersion is expected to increase of the sample resistance, due to the reduction of contact points between SWNTs [**51]**. This expectation is met by the data on resistance reported in **Table 1**. Indeed, while the resistance of the bare SWNTs was about 652 Ohm, MINTs samples displayed a resistance in the 1159-2829 Ohm range. Similar mechanisms were proposed in Ref. **[52]** where transport in SWNTs layers was discussed in terms of percolation, charge tunneling, and "quantum resistive" mechanisms. The increase of the overall sample resistance may lead to an increase in the ΔI/I (=ΔR/R) response of the system. This can also be explained by assuming that the sensing layers can be modelled in terms of bundles of SWNTs connected as a set of parallel resistances. This is discussed in more detail in the SI (Fig. S12 and related comments).

ii) The MINTs more efficient dispersion on the IDE surface with respect to bare SWNTs not only yields a higher sensing surface but also allows the gas to penetrate more efficiently into deeper layers and reach MINTs close to the charge-collecting IDE, thus reducing scattering along the conductive paths to IDE. This is demonstrated in Subsection 3.4 below.

Finally, iii) Functionalization may play a fundamental role regarding the increase of the sensing performance, but a rigorous assessment of this aspect requires a more systematic structure-activity investigation.

As for the apparent selectivity to target gas molecules (Fig.4), we observe that ammonia is the smallest among the considered gas molecules [**see, e.g., Ref. 53**]. Therefore, if mechanism (ii) mentioned above holds, then the larger response can be related to a more efficient diffusion of NH_3 from the surface of the sensing layer in close contact with the underneath IDE. A similar explanation can be assumed for NO_2, which in addition displays a strong interaction with the sensing layer, as compared to the other analytes, as shown in Fig.4. In this frame, the role of functionalization is still an open issue. Beyond this steric hindrance aspect, we cannot exclude that interaction of the different target gas molecules may

lead to a different extent of charge transfer and, therefore, selectively tune the response to some gases, but as mentioned above, the effectiveness of a specific functionalization to capture gas molecules and transfer charge still has to be demonstrated.

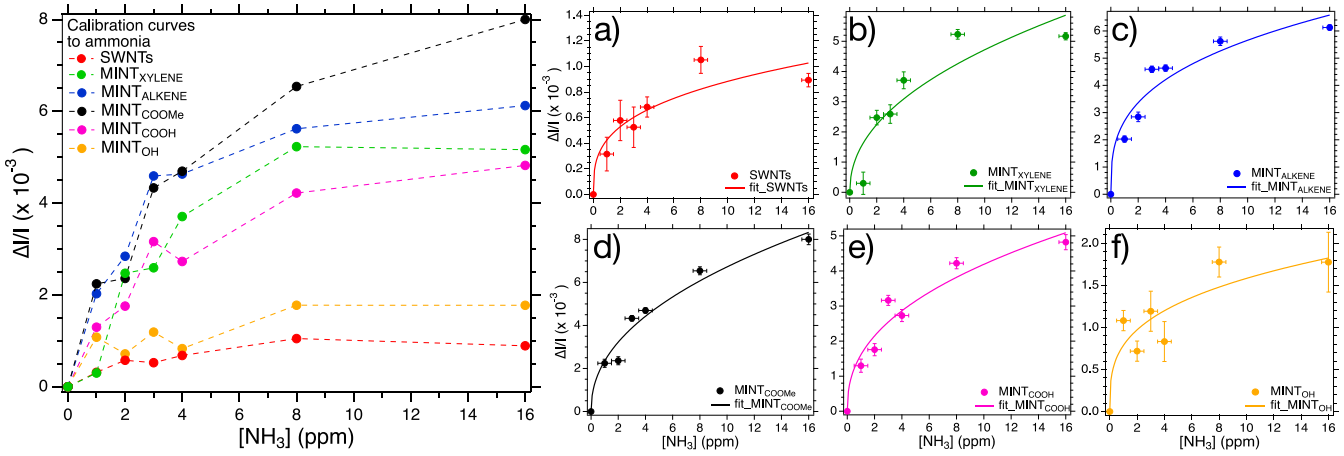

Figure 5. Left panel: calibration curves for exposure to NH_3 in the 1-16 ppm range. Lines have been drawn as a guide for the eyes. **Right panel:** Calibration curves for SWNTs (a), MINT$_{XYLENE}$ (b), MINT$_{ALKENE}$ (c), MINT$_{COOMe}$ (d) MINT$_{COOH}$ (e), MINT$_{OH}$ (f) and fit with Freundlich isotherms.

3.3 From single chemiresistors to an e-nose

In all gas exposures, the sensing layers responses were recorded simultaneously in a multi-channel signal readout scheme, thus enabling the driving of all devices in the array as an e-nose. Data were collected by exposing the e-nose to NH_3 and to the whole set of interfering gases. The sensor responses scatter plot matrix is shown in the upper diagonal part of **Figure 6-a**. Six clusters of data points are detectable, obtained after exposure to acetone (150 to 200 ppm), NH_3 (12-16 ppm), NaClO (40-50 ppm), EtOH (150 to 200 ppm), IPA (150 to 200 ppm), NO_2 (2-8 ppm). Panel b), extracted from one of the scatter plots of **Figure 6-a**, shows how it is possible to obtain a good discrimination of the contaminants just by using a couple of sensors. In this case, we chose two of the best performing ones: "MINT$_{XYLENE}$" and "MINT$_{COOH}$" sensing layers. Indeed, the six tracks of data points do not overlap, for the concentration ranges explored in the experiment. As the negative ΔI/I data points for acetone and ethanol are found above the diagonal line of Panel b), the "MINT$_{COOH}$" sensing layers displays a higher sensitivity to these target gas molecules than the "MINT$_{XYLENE}$" layer. In the case of IPA, both sensors display a similar behavior. Furthermore, discrimination of NH_3 and NaClO is mostly enabled by "MINT$_{COOH}$", while different concentrations of the same molecules are tracked by the "MINT$_{XYLENE}$" layer. Positive ΔI/I values are registered for NO_2, which make this analyte easily discriminated in all scatter matrix plots. As the response to NO_2 is quite large even at low concentrations, in all panels of Fig.6 data for NO_2 have been divided by 10 to make them visible on the ΔI/I value range used for all other analytes.

An improved discrimination can be achieved through a principal component analysis (PCA) of the same data set. PCA was performed on the sensor responses (ΔI/I) by using the scikit-learn python library. All data have been scaled before the transformation. The PCA matrix is shown in the lower part of **Figure 6-a**, while the PC1 vs. PC2 plot is shown in **Figure 6-**c. Indeed, the first two principal components carry 97% of the total variance (94.4% and 2.6%, respectively, **Table 2**) and, by plotting them, all 5 clusters result to be well separated from one another, occupying all areas of the PC1-PC2 panel, demonstrating that additional discrimination capability can be provided by using an e-nose architecture to data collection and analysis.

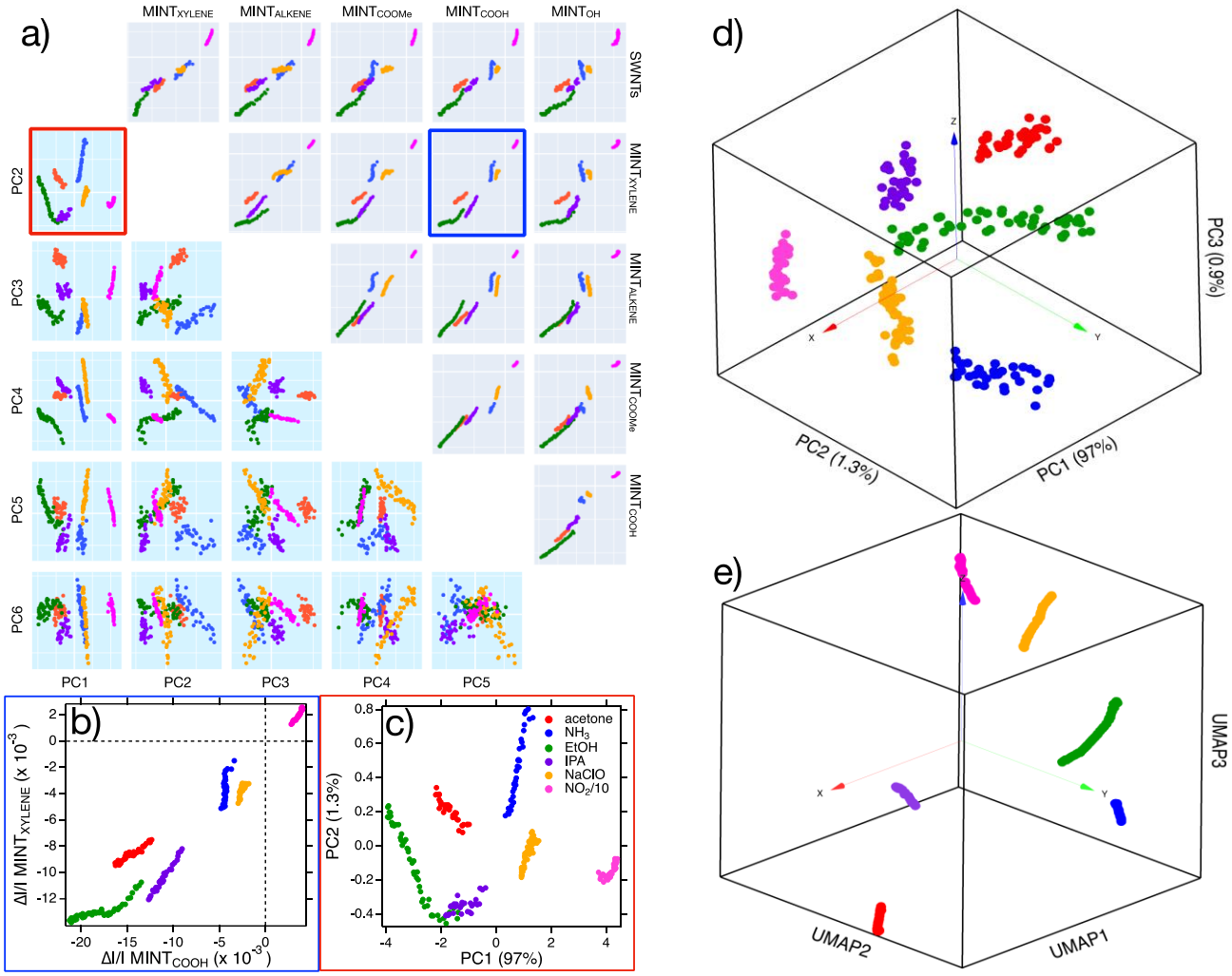

Figure 6: a) upper part: sensor responses scatter plot matrix; lower part: PCA dataset analysis. The dataset for each analyte was collected in the following concentrations ranges. Acetone: 150 to 200 ppm; NH_3: 12-16 ppm, NaClO: 40-50 ppm, EtOH: 150 to 200 ppm, IPA: 150 to 200 ppm; NO_2: 2-8 ppm (values scaled by a factor 0.1). b) response of "$MINT_{XYLENE}$" vs "$MINT_{COOH}$"; c) PC1 vs PC2 plot; d) PC1 vs PC2 vs PC3 plot; e) UMAP plot.

A 3D scatter plot showing PC1 vs PC2 vs PC3 is shown in **Figure 6-d**. Adding a further axis enhances even more the discrimination of the contaminants, displaying a clear separation among the target gas molecules.

Finally, in **Figure 6-e** we show that cluster visualization can be further improved with other dimensionality reduction techniques. More specifically, we used the Uniform Manifold Approximation and Projection (UMAP), which reduces dimensions of a graph (from 6 to 3, in the present case), by maintaining the features of the high-dimensional clusters, such as the distance between the points. Therefore, while UMAP analysis helps exploring the multidimensional dataset space, searching for clusters, and improving data representation in lower dimensional space, PCA provides interpretable results, as the principal components represent linear combinations of the original features. Therefore, in the present case, PCA is helpful to discuss the role of each sensing layer in the discrimination of target gas molecules. Indeed, further comments on the PCA discrimination capability can be drawn by the outcome of the PCA analysis, reported in **Table 2**. The first two principal components account for 97% percent of the total dataset variance (right column), cumulative variance) and almost 95% is ascribed to PC1. This guarantees the best clustering performance by using only the first two components of the six available. Loadings contain much information. One can notice that PC1 is composed of an approximately equal amount of all the six responses, each one contributing with a weight of 16%. Regarding PC2, the situation is different. In fact, in this case the contribution of $MINT_{ALKENE}$ and $MINT_{COOH}$ are lower than 10%. On the other hand, $MINT_{XYLENE}$ and $MINT_{COOH}$ play an important role, with weights equal to 40% and 30% respectively. These values are followed by pristine and MeOH, with weights values of approximately 16%.

These results show that, though two selected sensors can be used to achieve a discrimination of most analytes, the combination of PCA and UMAP analysis further improves the result, the first analysis being able to show that all sensors contribute to the discrimination improvement (see loadings for PC1), the second to provide an effective representation of clusters.

In view of possible applications of this e-nose, we explored a typical case where the e-nose can be used for sensing in breathomics. The focus on ammonia will help us to discuss whether ammonia can be discriminated over a background of interfering gases and, in particular when ammonia is expected to be found coupled with

other biomarkers in specific diseases. Therefore, we proceed to analyze the cases of three possible gas mixtures involving three biomarkers considered so far (acetone, ethanol, and isopropyl alcohol). In particular the first mixture was built considering NH_3 and ethanol, as both biomarkers are known to be present in the exhaled breath analysis and allows for an assessment of gastrointestinal physiology conditions **[54]**. For this first case, we have built the response to a mixture of NH_3 and ethanol (50%, 50%). With the aim to see how and where mixture data clusters are positioned with respect to the single gases, data have been properly normalized and carried into the principal components space as unknown data to be classified with the PCA settings obtained from the analysis of single molecule classification shown in **Fig.6**.

As can be observed in Fig.7, the PCA analysis allows us to classify the signal from the mixture that appears as an isolated cluster in the PC1-PC2-PC3 space. This cluster indicates that in case of simultaneous presence of both analytes, a cluster is expected in the space between the NH_3 and the ethanol clusters. The mixture cluster is easily detectable and well separated from those of the single target molecules, showing that when the discrimination of the two initial gas molecules is effective (i.e. their clusters are well separated as in **Fig.6**) then the mixture can be effectively recognized. Similar results are obtained for ethanol and acetone, as well as for isopropanol and acetone. These further results are shown in Fig. S13 of the SI file. The concentrations of ethanol and acetone in the exhaled breath can be related to diabetes, as acetone and ethanol are indicators of serum glucose levels **[55]**. In turn, isopropanol and acetone have been targeted by Li et al. in [**56]** who explored the correlations between exhaled IPA and acetone with the aim to evaluate diabetes diagnostic applicability of exhaled IPA in combination with acetone.

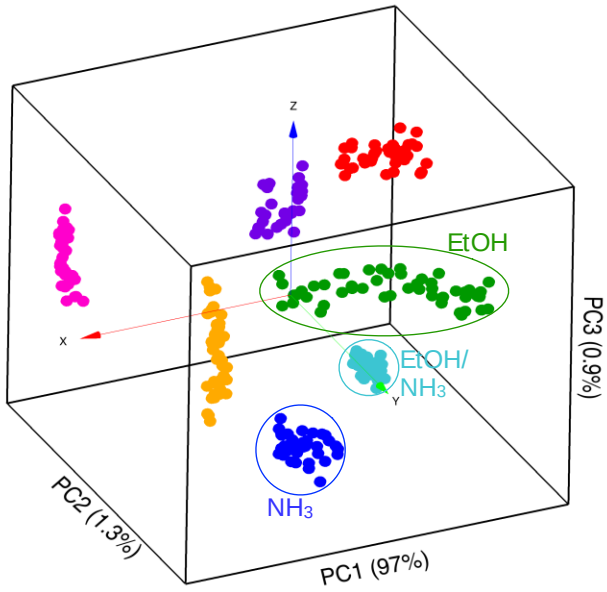

Figure 7: Results of the PCA classification of an EtOH/NH_3 mixture. To help viewing the different target gas molecules and the mixture, clusters have been evidenced by shaded ellipses.

Table 2: PCA loadings for the six sensing layers, relative variance and cumulative value of the principal components.

	PCA loadings						PCA variances	
	SWNTs	$MINT_{XYLENE}$	$MINT_{ALKENE}$	$MINT_{COOMe}$	$MINT_{COOH}$	$MINT_{OH}$	% variance	cumulative % variance
PC1	0.41	0.41	0.41	0.41	0.41	0.41	97.0%	97.0%
PC2	0.14	0.65	0.20	-0.46	0.05	-0.56	1.3%	98.3%
PC3	0.68	0.15	-0.50	0.17	-0.48	-0.02	0.9%	99.1%
PC4	-0.04	0.11	-0.70	-0.04	0.70	-0.04	0.5%	99.7%
PC5	-0.48	0.39	-0.12	0.69	-0.19	-0.29	0.2%	99.9%
PC6	-0.33	0.48	-0.19	-0.34	-0.27	0.66	0.1%	100.0%

3.4 Strategies for sensitivity and dynamic response improvement.

So far, sensors have been produced by dropcasting small amounts of solution on the substrate and continue with other layers after the solvent evaporated from the previous one ("multilayer" samples). MINTs-based chemiresistor performances have been further improved by tuning the deposition parameters. Indeed, for one of the best performing layers ($MINT_{ALKENE}$) we introduced a different layer deposition procedure. We dropcasted a precise amount of solution, 30uL, "all at once" thus obtaining a single deposition sensing layer (hereafter denoted as "monolayer" sample). Indeed, without modifying MINTs solution or experimental setup, it was possible to increase to response up to one order of magnitude.

At the end, the reduced thickness greatly improved the response dynamics. The results are shown in **Figure 8**. We compared two chemiresistors, one monolayer $MINT_{ALKENE}$ and one multilayer $MINT_{ALKENE}$. Experimental setup and conditions are exactly the same of the formerly presented exposures. Panel (a) displays the comparison between the dynamic responses obtained with monolayer and multilayer $MINT_{ALKENE}$ chemiresistors by exposing them to acetone, NH_3, EtOH, IPA, NaClO and water. Panels (b) to (g) show the normalised responses to one gas exposure. It is clear that in all cases monolayer sample completely

outperforms multilayer one, both in response and times. Responses are presented in the bar graph in panel (h), including their ratio too. It is important to notice that sensing ethanol and IPA with monolayer $MINT_{ALKENE}$ yields a response almost 10 times higher than multilayer one, while with NaClO this ratio reaches a value of 30. Regarding the dynamic behavior, presented in panel (i) and (j) for response and recovery time respectively, monolayer $MINT_{ALKENE}$ exhibits a response time lower than 10 seconds for each target gas. It also displays lower recovery time values than the multilayer. Overall, with this sensing layer deposition procedure, response and recovery times in the dynamic response is significantly reduced and response can be significantly enhanced.

4. Conclusions

An array of MINT-based chemiresistors has been prepared for the selective detection of VOCs. The functionalized sensing layers have been tested by exposing them to NH_3, EtOH, IPA, benzene, NO_2, acetone, and NaClO vapors in the 10-200 ppm range. The response to analytes results to be enhanced with respect to bare SWNTs by MINT functionalization. When assembled into an array, the sensing layers were able to operate as an electronic nose, disclosing the possibility to discriminate a specific analyte (NH_3 in the present case) with respect to other possible interfering volatiles. In fact, response scatter plots, PCA and UMAP analysis showed that a discrimination of NH_3 with respect to interfering gases can be achieved. The present study represents a proof-of-concept, but the physical system selected to build the sensing layers offers a large set of parameters to optimize and increase the sensitivity of single layers and the overall discrimination capability. Indeed, an effective improvement of detection performance has been shown for one of the best-performing layers, where the thickness reduction has led up to a 10-fold increase of sensitivity and to a remarkable reduction of response and recovery time.

More generally, we show that MINTs are an attractive material to build chemiresistive sensors, consistently outperforming non-functionalized SWNTs. The flexibility of the synthetic methods towards MINTs permits a large degree of structural variation on the macrocycles, opening an interesting new avenue for the design of SWNT-based sensors.

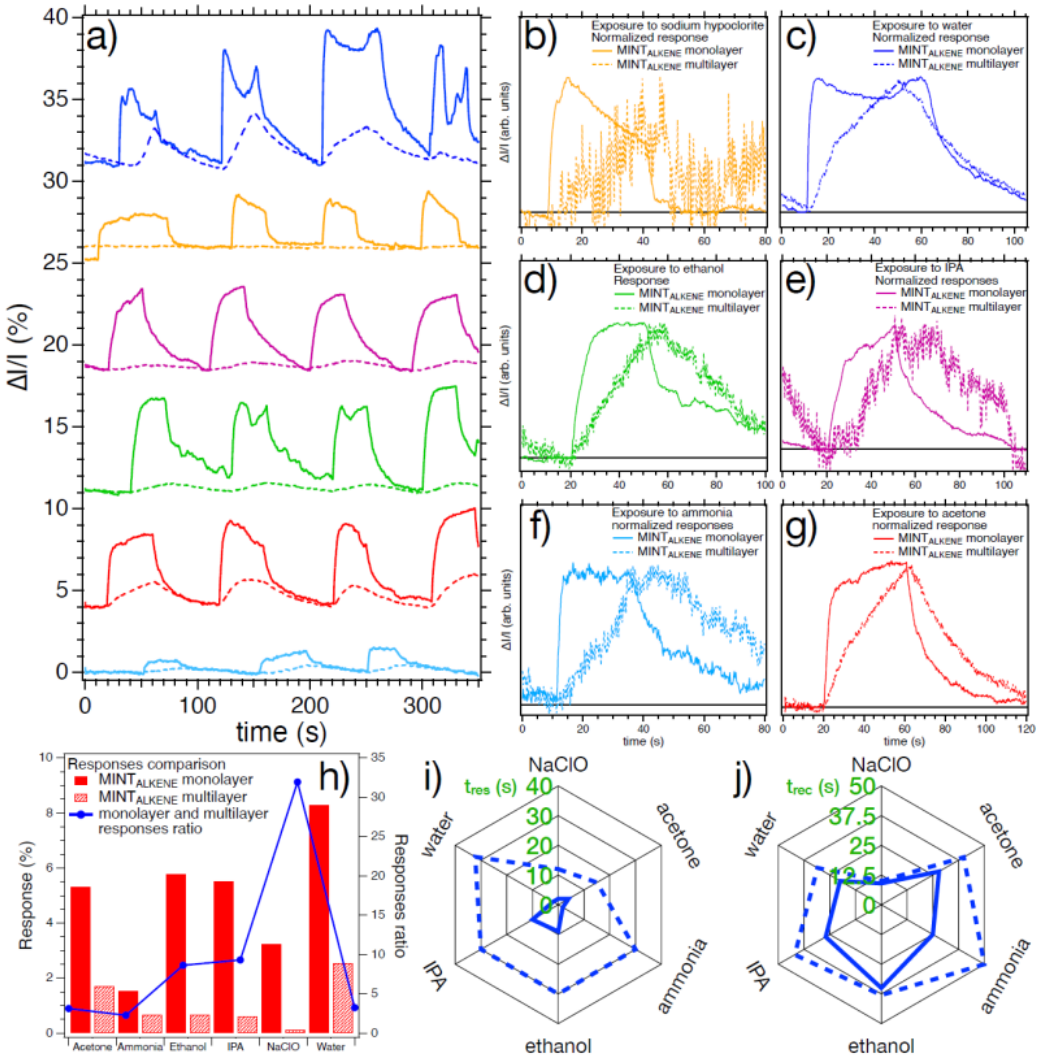

Figure 8: a) Dynamic responses of monolayer $MINT_{ALKENE}$ (solid lines) and multilayer $MINT_{ALKENE}$ (dashed lines) during exposures to contaminant gases. b) to g) Details of single exposures to the six analytes. In these graphs traces have been normalised to ease the comparison; h) responses bar graph and response ratio (single layer / multilayer); i) response time spider plot. Monolayer $MINT_{ALKENE}$ is represented by a solid line, multilayer $MINT_{ALKENE}$ by a dashed line; j) recovery time spider plot

ASSOCIATED CONTENT

Supporting Information

Supplementary information, containing all the supplementary figures and text, and experimental data on Ushapes and MINTs synthesis specifications and characterization (NMR, TGA and UV-vis-NIR and Raman spectra.

ACKNOWLEDGMENTS
E.M.P. acknowledges funding from the Ministerio de Ciencia, Innovación y Universidades (PID2023-152267NB-I00), and Comunidad de Madrid "Materiales Disruptivos Bidimensionales (2D)" (MAD2D-CM)-UAM and (MAD2D-CM)-IMDEA-NC funded by the Recovery, Transformation and Resilience Plan, and by NextGenerationEU from the European Union. IMDEA Nanoscience acknowledges support from the ''Severo Ochoa'' Programme for Centres of Excellence in R&D CEX2020-001039-S.

M.G. acknwoledges support from the PNRR-DM352 2022 funding scheme of the Italian Ministero dell'Università e della Ricerca (MUR) and by Antares Vision Group.

REFERENCES

1. Schroeder, V.; Savagatrup, S.; He, M.; Lin, S.; Swager, T.M. Carbon Nanotube Chemical Sensors. *Chem. Rev.* **2019**, 119(1), 599–663.

2. Huang, X.; Pang, R.; Yang, M.; Zhang, S.; Guo, F.; Xu, J.; Zhang, Y.; Cao, A.; Shang, Y. Flexible Gas Sensors Based on Carbon Nanotube Hybrid Films: A Review. *Advanced Materials Technologies*, **2023**, 8(21), 2300616.

3. Galvani, M.; Freddi, S.; Sangaletti, L. Disclosing fast detection opportunities with nanostructured chemiresistor gas sensors based on metal oxides, carbon, and transition metal dichalcogenides. *Sensors*, **2024**, 24(2), 584.

4. Zamansky, K.K.; Fedorov, F.S.; Shandakov, S.D.; Chetyrkina, M.; Nasibulin, A.G. A gas sensor based on free-standing SWNT film for selective recognition of toxic and flammable gases under thermal cycling protocols *Sensors and Actuators B: Chemical*, **2024**, 417,136116.

5. Freddi, S.; Drera, G.; Pagliara, S.; Goldoni, A.; Sangaletti, L. Enhanced selectivity of target gas molecules through a minimal array of gas sensors based on nanoparticle-decorated SWNTs. *Analyst*, **2019**, 144, 4100-4110.

6. Zhang, T.; Ren, W.; Xiao, F.; Li, J.; Zu, B.; Dou, X. Engineered olfactory system for in vitro artificial nose. *Eng. Regen.*, **2022**, 4, 427-439.

7. Singh, P.; Campidelli S.; Giordani, S.; Bonifazi, D.; Bianco, A.; Prato, M. Organic functionalisation and characterisation of single-walled carbon nanotubes, *Chem. Soc. Rev.*, **2009**, 38, 2214 -2230.

8. Zhao, Y.-L.; Stoddart, J. F. Noncovalent functionalization of single-walled carbon nanotubes. *Acc. Chem. Res.* **2009**, 42 (8), 1161- 1171.

9. Luo, S.X.L.; Swager, T.M. Chemiresistive sensing with functionalized carbon nanotubes. *Nat. Rev. Methods Primers*, **2023**, 3(1), 73.

10. Kauffman, D.R.; Sorescu, D.C.; Schofield, D.P.; Allen, B.L.; Jordan, K.D.; Star, A. Understanding the Sensor Response of Metal-Decorated Carbon Nanotubes. *Nano Letters*, **2010**, 10, 958-963.

11. López-Moreno, A.; Villalva, J.; Pérez, E.M. Mechanically interlocked derivatives of carbon nanotubes: synthesis and potential applications. *Chem. Soc. Rev*., **2022**, 51(23), 9433-9444.

12. López-Moreno, A.; Pérez, E. M., Mechanically Interlocked Nanotubes. In Mechanically Interlocked Materials, 2024; pp 83-103.

13. Mena-Hernando, S.; Eaton, M.; Fernández-Blázquez, J.P.; López-Moreno, A.; Pedersen, H.; Pérez, E.M. Mechanical interlocking to unlock the reinforcing potential of carbon nanotubes. *Chem. Eur. J.*, **2023**, *29*(58), e202301490.

14. Villalva, J.; Rapakousiou, A.; Monclús, M. A.; Fernández Blázquez, J. P.; de la Vega, J.; Naranjo, A.; Vera-Hidalgo, M.; Ruiz-González, M. L.; Pedersen, H.; Pérez, E. M. Interlocking Matrix and Filler for Enhanced Individualization and Reinforcement in Polymer–Single-Walled Carbon Nanotube Composites, *ACS Nano*, **2023**, 17, 16565-16572.

15. Isasti, I.; Miranda, S.; Jiménez, D. M.; Parzyszek, S.; Martín Sabanés, N.; Pedersen, H.; Pérez, E. M. Reinforcement of Polyimine Covalent Adaptable Networks with Mechanically Interlocked Derivatives of SWNTs. *Adv. Funct. Mater.* **2024**, 34, 2408592.

16. Moreno-Da Silva, S.; Martínez, J.I.; Develioglu, A.; Nieto-Ortega, B.; de Juan-Fernández, L.; Ruiz-Gonzalez, L.; Picón, A.; Oberli, S.; Alonso, P.J.; Moonshiram, D.; Pérez, E.M. Magnetic, mechanically interlocked porphyrin–carbon nanotubes for quantum computation and spintronics. *J. Am. Chem. Soc.* **2021**, 143(50), 21286-21293.

17. Blanco, M.; Nieto-Ortega, B.; de Juan, A.; Vera-Hidalgo, M.; López-Moreno, A.; Casado, S.; González, L.R.; Sawada, H.; González-Calbet, J.M.; Pérez, E.M. Positive and negative regulation of carbon nanotube catalysts through encapsulation within macrocycles. *Nat. Commun.* **2018**, 9(1), 2671.

18. Wielend, D.; Vera-Hidalgo, M.; Seelajaroen, H.; Sariciftci, N.S.; Pérez, E.M.; Whang, D.R. Mechanically interlocked carbon nanotubes as a stable electrocatalytic platform for oxygen reduction. *ACS Appl. Mater. Interfaces*, **2020**, 12(29), 32615-32621.

19. Zhang, W. Z.; Guillén-Soler, M.; Moreno-Da Silva, S.; López-Moreno, A.; González, L. R.; Giménez-López, M. D.; Pérez, E. M. Mechanical interlocking of SWNTs with N-rich macrocycles for efficient ORR electrocatalysis, *Chem. Sci.*, **2022**, 13, 9706- 9712.

20. Pérez, E. M. Putting Rings around Carbon Nanotubes, *Chem. Eur. J.* **2017**, 23, 12681.

21. Miki, K.; Saiki, K.; Umeyama, T.; Baek, J.; Noda, T.; Imahori, H.; Sato, Y.; Suenaga, K.; Ohe, K. Unique Tube–Ring Interactions: Complexation of Single-Walled Carbon Nanotubes with Cycloparaphenyleneacetylenes, *Small*, *2018*, 14, 1800720.

22. Cheng, G.; Hayashi, T.; Miyake, Y.; Sato, T.; Tabata, H.; Katayama, M.; Komatsu, N. Interlocking of Single-Walled Carbon Nanotubes with Metal-Tethered Tetragonal Nanobrackets to Enrich a Few Hundredths of a Nanometer Range in Their Diameters, *ACS Nano*, **2022**, 16, 8, 12500–12510.

23. López-Moreno, A.; Ibáñez, S.; Moreno-Da Silva, S.; Ruiz-González, L.; Martín Sabanés, N.; Peris, E.; Pérez, E. M. Single-Walled

Carbon Nanotubes Encapsulated within Metallacycles, Angew. *Chem. Int. Ed.* **2022**, 61, e202208189.

24. Balakrishna, B.; Menon, A.; Cao, K.; Gsänger, S.; Beil, S. B.; Villalva, J.; Shyshov, O.; Martin, O.; Hirsch, A.; Meyer, B.; Kaiser, U.; Guldi, D. M.; von Delius, M. Dynamic covalent formation of concave disulfide macrocycles mechanically interlocked with single-walled carbon nanotubes, Angew. *Chem. Int. Ed*. **2020**, 59, 18774.

25. Kraus, J.; Meingast, L.; Hald, J.; Beil, S. B.; Biskupek, J.; Ritterhoff, C. L.; Gsänger, S.; Eisenkolb, J.; Meyer, B.; Kaiser, U.; Maultzsch, J.; von Delius, M. Simultaneous Inside and Outside Functionalization of Single-Walled Carbon Nanotubes, *Angew. Chem. Int. Ed*. **2024**, 63, e202402417.

26. Naranjo, A.; Jiménez, D. M.; Rivas-Caramés, M.; Villalva, J.; Ruiz-González, M. L.; Pedersen, H.; López-Moreno, A.; Pérez, E. M. Multigram Scale Synthesis of Mechanically-Interlocked Derivatives of SWNT using Mechanochemical Methods, *Chem. Eur. J.* **2025**, 31, e202404762.

27. Tanaka, K.; Cheng, G.; Nakamura, T.; Hiraoka, K.; Tabata, H.; Kubo, O.; Komatsu, N.; Katayama, M. NH3 Gas Sensors Based on Single-Walled Carbon Nanotubes Interlocked with Metal-Tethered Tetragonal Nanobrackets. *ACS Appl. Nano Mater*. **2024**, 7, 11, 13417–13425.

28. Li, M.; Weschler, C.J.; Beko, G.; Wargocki, P., Lucic, G.; Williams, J. Human ammonia emission rates under various indoor environmental conditions. *Environ. Sci. Technol*. **2020**, 54(9), 5419-5428.

29. Chiesa, M., Rigoni, F., Paderno, M., Borghetti, P., Gagliotti, G., Bertoni, M.; Ballarin Denti, A.; Schiavina, L.; Goldoni, A.; Sangaletti, L. Development of low-cost ammonia gas sensors and data analysis algorithms to implement a monitoring grid of urban environmental pollutants. *J. Environ. Monit,* **2012**, 14, 1565-1575.

30. Ellis, J.E.; Star, A. Carbon Nanotube-based Gas Sensors toward Breath Analysis, *ChemPlusChem*, **2016**, 81, 1248-1265.

31. Luo, S.X.L.; Swager, T.M. Wireless Detection of Trace Ammonia: A Chronic Kidney Disease Biomarker. *ACS Nano*, **2023**, 18(1), 364-372.

32. Freddi, S.; Emelianov, A.V.; Bobrinetskiy, I.I.; Drera, G.; Pagliara, S.; Kopylova, D.S.; Chiesa, M.; Santini, G.; Mores, N.; Moscato, U.; Nasibulin, A.G.; Montuschi, P.; Sangaletti, L. Development of a sensing array for human breath analysis based on SWNT layers functionalized with semiconductor organic molecules. *Adv. Healthc. Mater.* **2020**, 9, 2000377.

33. Freddi, S.; Sangaletti, L. Trends in the Development of Electronic Noses Based on Carbon Nanotubes Chemiresistors for Breathomics, *Nanomaterials*, **2022**, 12, 2992.

34. Ionescu, R.; Broza, Y., Shaltieli, H.; Sadeh, D.; Zilberman, Y.; Feng, X.; Glass-Marmor, L.; Lejbkowicz, I.; Müllen, K.; Miller, A.; Haick, H. Detection of multiple sclerosis from exhaled breath using bilayers of polycyclic aromatic hydrocarbons and single-wall carbon nanotubes. *ACS Chem. Neurosci.* **2011**, 2(12), 687-693.

35. Spacek, L. A.; Mudalel, M. L.; Lewicki, R.; Tittel, F. K.; Risby, T. H.; Stoltzfus, J.; Munier, J. J.; Solga, S. F. Breath ammonia and ethanol increase in response to a high protein challenge. *Biomarkers*, **2015**, 20(2), 149–156.

36. Galassetti, P.R.; Novak, B.; Nemet, D; Rose-Gottron, C.; Cooper, D. M.; Meinardi, S.; Newcomb, R.; Zaldivar, F.; Blake D. R. Breath ethanol and acetone as indicators of serum glucose levels: an initial report. *Diabetes Technol Ther.* **2005,** 7(1), 115-23.

37. Li, W.; Liu, Y.; Liu, Y.; Cheng, S.; Duan, Y. Exhaled isopropanol: new potential biomarker in diabetic breathomics and its metabolic correlations with acetone, *RSC Adv.*, **2017**, 7, 17480-17488.

38. see, e.g., Chapter 14 in "The Elements of Statistical Learning" by Trevor Hastie, Robert Tibshirani, and Jerome Friedman, Springer (Berlin) 2003.

39. McInnes, L.; Healy, J.; & Melville, J. Umap: Uniform manifold approximation and projection for dimension reduction. **2018** *arXiv preprint arXiv:1802.03426*.

40. Zahab, A.; Spina, L.; Poncharal, P. Water-vapor effect on the electrical conductivity of a single-walled carbon nanotube mat. *Phys. Rev. B.* **2000**, 62, 10000.

41. Rigoni, F.; Drera, G.; Pagliara, S.; Goldoni, A.; Sangaletti, L. High sensitivity, moisture selective, ammonia gas sensors based on single-walled carbon nanotubes functionalized with indium tin oxide nanoparticles. *Carbon*, **2014**, 80, 356-363.

42. Z. Chen et al., Advancing Breathomics through Accurate Discrimination of Endogenous from Exogenous Volatiles in Breath, Environ. Sci. Technol. 2024, 58, 42, 18541–18553.

43. F. Tournus and J.-C. Charlier, Ab initio study of benzene adsorption on carbon nanotubes, PHYSICAL REVIEW B 71, 165421 (2005).

44. Dresselhaus, M.S.; Dresselhaus, G.; Saito, R.; Jorio, A. Raman spectroscopy of carbon nanotubes. *Phys. Rep.* **2005**, 409, 47-99.

45. Jorio, A.; Saito, R. Raman spectroscopy for carbon nanotube applications. *J. Appl. Phys.* **2021**, 129, 021102.

46. Tuball^{tm} graphene nanotubes; https://tuball.com/about-tuball.

47. Gupta, S.; Anand, A.; Neeru; Kumar, R. Analytical modeling of adsorption isotherms for pristine and functionalized carbon nanotubes as gas sensors. *Int. J. Mater.*, **2023**, 114(7-8), 653-661.

48. Sheindorf, C.H.; Rebhun, M.; Sheintuch, M. A Freundlich-type multicomponent isotherm. *J. Colloid Sci.*, **1981**, 79(1), 136-142.

49. Rigoni, F.; Freddi, S.; Pagliara, S.; Drera, G.; Sangaletti, L.; Suisse, J-M.; Bouvet, M.; Malovichko, A. M.; Emelianov, A. V.; Bobrinetskiy, I. I. Humidity-enhanced sub-ppm sensitivity to ammonia of covalently functionalized single-wall carbon nanotube bundle layers, *Nanotechnology*, **2017**, 28, 255502.

50. Shirvani, B. B.; Beheshtian, J.; Parsafar, G.; Hadipour, N. L. DFT study of $NH_3(H_2O)_n$=0,1,2,3 complex adsorption on the (8, 0) single-walled carbon nanotube, *Comput. Mater. Sci.* **2010**, 48, 655–657.

51. Battie, Y.; Gorintin, L.; Ducloux, O.; Thobois, P.; Bondavalli, P.; Feugnetb, G.; Loiseau, A. Thickness dependent sensing mechanism in sorted semi-conducting single walled nanotube based sensors. *Analyst*, **2012**, 137, 2151.

52. Tripathi, K.M.; Sachan, A.; Castro, M.; Choudhary, V.; Sonkar, S.K.; Feller, J.F. Green carbon nanostructured quantum resistive

sensors to detect volatile biomarkers. *Sustain. Mater. Technol*. **2018**, 16, 1-11.

53. Marcus, Y. The sizes of molecules—revisited, J. Phys. *Org. Chem.* **2003**; 16: 398–408.

Insert Table of Contents artwork here